IPEM Institute of Physics and Engineering in Medicine

PAPER

Evaluation of ^{209}At as a theranostic isotope for ^{209}At-radiopharmaceutical development using high-energy SPECT

To cite this article: J R Crawford et al 2018 Phys. Med. Biol. **63** 045025

View the article online for updates and enhancements.

Related content

Physics in Medicine & Biology

IPEM Institute of Physics and Engineering in Medicine

CrossMark

PAPER

Evaluation of 209At as a theranostic isotope for 209At-radiopharmaceutical development using high-energy SPECT

J R Crawford[1,2,3,8], A K H Robertson[1,4,8] [iD], H Yang[1], C Rodríguez-Rodríguez[4,5], P L Esquinas[6], P Kunz[7], S Blinder[4], V Sossi[4], P Schaffer[1,6] and T J Ruth[1,3]

1   Life Sciences Division, TRIUMF, 4004 Wesbrook Mall, Vancouver BC, V6T 2A3, Canada
2   Molecular Oncology, BC Cancer Research Centre, 675 W 10th Ave, Vancouver BC, V5Z 1L3, Canada
3   Department of Physics and Astronomy, University of Victoria, PO Box 1700 STN CSC, Victoria BC, V8W 2Y2, Canada
4   Department of Physics and Astronomy, University of British Columbia (UBC), 6224 Agronomy Road, Vancouver BC, V6T 1Z1, Canada
5   Centre for Comparative Medicine, University of British Columbia (UBC), 4145 Wesbrook Mall, Vancouver BC, V6T 1W5, Canada
6   Department of Radiology, University of British Columbia, 3350-950 W 10th Ave, Vancouver BC, V5Z 4E3, Canada
7   Accelerator Division, TRIUMF, 4004 Wesbrook Mall, Vancouver BC, V6T 2A3, Canada
8   Equal contributors.

E-mail: jcrawford@bccrc.ca

Keywords: astatine-211, astatine-209, theranostic pair, preclinical imaging, SPECT

Abstract

The development of alpha-emitting radiopharmaceuticals using ^{211}At requires quantitative determination of the time-dependent nature of the ^{211}At biodistribution. However, imaging-based methods for acquiring this information with ^{211}At have not found wide-spread use because of its low abundance of decay emissions suitable for external detection. In this publication we demonstrate the theranostic abilities of the ^{211}At/^{209}At isotope pair and present the first-ever ^{209}At SPECT images.

The VECTor microSPECT/PET/CT scanner was used to image ^{209}At with a collimator suitable for the 511 keV annihilation photons of PET isotopes. Data from distinct photopeaks of the ^{209}At energy spectrum (195 keV (22.6%), 239 keV (12.4 %), 545 keV (91.0 %), a combined 782/790 keV peak (147 %), and ^{209}Po x-rays (139.0 %)) were independently evaluated for use in image reconstructions using Monte Carlo (GATE) simulations and phantom studies. ^{209}At-imaging *in vivo* was demonstrated in a healthy mouse injected with 10 MBq of free [^{209}At]astatide. Image-based measurements of ^{209}At uptake in organs of interest—acquired in 5 min intervals—were compared to *ex vivo* gamma counter measurements of the same organs.

Simulated and measured data indicated that—due to the large amount of scatter from high energy ($>$750 keV) gammas—reconstructed images using the x-ray peak outperformed those obtained from other peaks in terms of image uniformity and spatial resolution, determined to be $<$0.85 mm. ^{209}At imaging using the x-ray peak revealed a biodistribution that matched the known distribution of free astatide, and *in vivo* image-based measurements of ^{209}At uptake in organs of interest matched *ex vivo* measurements within 10%.

We have acquired the first ^{209}At SPECT images and demonstrated the ability of quantitative SPECT imaging with ^{209}At to accurately determine astatine biodistributions with high spatial and temporal resolution.

1. Introduction

Targeted alpha therapy (TAT) combining alpha-emitting radionuclides with disease-targeting biomolecules has shown great promise for the treatment of advanced and aggressive cancers and is an active area of research (McDevitt *et al* 1998, Couturier *et al* 2005, Mulford *et al* 2005, Brechbiel 2007, Kim and Brechbiel 2012, Baidoo *et al* 2013, Elgqvist *et al* 2014). ^{211}At is one of the few isotopes suitable for use in these radiopharmaceuticals, favourable due to its 7.2 h half-life that provides sufficient time for preparation of the pharmaceutical and targeting of the cancer once in the body. Results from preclinical and clinical trials have demonstrated this

Table 1. Gamma and x-ray emissions resulting from the decay of ^{209}At and ^{211}At. ^{209}At emissions with branching ratio <5% or energy <70 keV are excluded. Data obtained from NNDC (National Nuclear Data Center 2017).
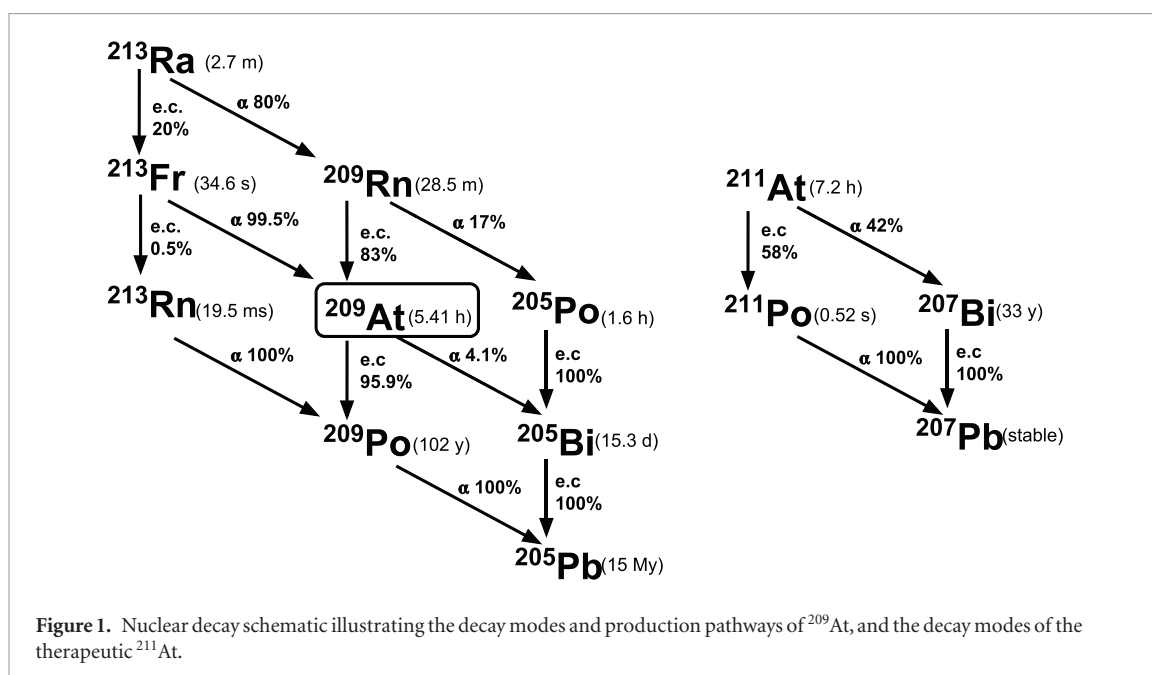
^{209}At		^{211}At	
Energy (keV)	Intensity (%/decay)	Energy (keV)	Intensity (%/decay)
77	36.3	77	12.4
79	60.0	79	20.7
89	7.3	89	2.5
90	15.8	90	4.9
92	5.2	92	1.8
x-rays (total)	124.6	x-rays (total)	42.3
195	22.6	570 (^{211}Po)	0.5
239	12.4	687	0.26
545	91.0	898 (^{211}Po)	0.5
782	83.5		
790	63.5		
1103	5.4		

isotope's potential for TAT (Bloomer *et al* 1981, Zalutsky *et al* 2008, Andersson *et al* 2009, Orozco *et al* 2013), though much of ^{211}At-radiopharmaceutical development remains in the early stages.

Crucial to the development of an ^{211}At -radiotherapeutic is an understanding of its time-dependent biodistribution. Such information regarding the uptake within the targeted cancerous or healthy tissues informs on the therapeutic effect and normal tissue toxicity of the radiopharmaceutical in question. For many isotopes in preclinical trials, this information is easily provided *in vivo* by SPECT or PET imaging, methods often complemented by *ex vivo* whole-organ counting of excised organs post-sacrifice. Therapeutic isotopes (alpha, beta, or Auger emitters) that also have gamma emissions sufficient for diagnostic SPECT or PET imaging can potentially be used as theranostics (ex. ^{213}Bi). A therapeutic isotope and a diagnostic isotope of the same element can also form a theranostic pair (ex. ^{124}I and ^{131}I). As a result of their identical chemical behaviour, the diagnostic isotope indicates the biodistribution of the therapeutic isotope. Radiolabelling with similar but different elements can also be used as theranostic pairs (e.g. ^{177}Lu and ^{68}Ga, or ^{211}At and ^{123}I); however the distinct chemical properties between the elements must be considered and interpreted for these pairs to be used as effective theranostic tools.

While first demonstrated in 1993 by Turkington *et al* (1993) and Johnson *et al* (1995), and later utilized in phase I clinical trials (Zalutsky *et al* 2008, Andersson *et al* 2009), quantitative SPECT imaging with ^{211}At is limited by the low intensity of its photon emissions and the relatively low activity concentrations in practical therapeutic applications. Complementary to SPECT, alpha-camera imaging has also been used to determine ^{211}At biodistributions at the sub-organ scale (Back and Jacobsson 2010, Chouin *et al* 2012, Back *et al* 2014, Miller *et al* 2014, 2015). Due to the short 65 μm range of ^{211}At alpha particles, this level of detail regarding the ^{211}At biodistribution is required to conduct ^{211}At dosimetry (Sgouros *et al* 2010, 2011). Unfortunately, this imaging method requires time-consuming and careful sample preparation and is limited to *ex vivo*, planar imaging. *Ex vivo* methods for determining biodistribution data are also limited by their inability to reveal the time-dependence of ^{211}At uptake within an organ (a time-activity curve or TAC) without using many animal subjects. Despite the progress made regarding SPECT and alpha-camera imaging of ^{211}At, new methods that can easily and accurately determine ^{211}At biodistribution information with high spatial and temporal resolution would assist the development of ^{211}At-radiopharmaceuticals.

Another astatine isotope, ^{209}At, has x-ray emissions more favourable for SPECT imaging compared to ^{211}At table 1 (Turkington *et al* 1993, Johnson *et al* 1995). As ^{209}At x-rays are three times more intense, they potentially provide a higher sensitivity signal. ^{209}At also has medium-energy gamma emissions 195 keV (22.6%), 239 keV (12.4%), and 545 keV (91.0%) that have potential for SPECT imaging. However, ^{209}At also has more intense high energy gamma emissions that are expected to produce large amounts of scattered photons that will potentially interfere with and corrupt lower-energy photopeaks—such effects have been observed for imaging ^{123}I in the presence of ^{124}I impurities, (Polak *et al* 1984, Macey *et al* 1986, Gilland *et al* 1991), and ^{188}Re (Esquinas *et al* 2017). In addition, ^{209}At decay figure 1 produces longer-lived daughters ^{205}Bi (gamma emitter) and ^{209}Po (alpha emitter); however, effective dose contributions from these decay products is negligible due to their distinct half-lives: 1 MBq of ^{209}At corresponds <1 kBq ^{205}Bi and <10 Bq ^{209}Po. ^{205}Bi is primarily a gamma emitter and does not contribute significantly to effective dose compared to ^{209}At. ^{209}Po is an alpha emitter with toxicity presumably comparable to ^{210}Po. For preclinical imaging applications, the amount of ^{209}Po resulting from ^{209}At injection is negligible but can potentially be an important consideration with respect to longitudinal studies.

Figure 1. Nuclear decay schematic illustrating the decay modes and production pathways of ^{209}At, and the decay modes of the therapeutic ^{211}At.

In this study, we evaluate ^{209}At as a novel SPECT isotope, using high energy collimation to preserve the integrity of lower energy photopeaks. Distinct photopeaks of the ^{209}At energy spectrum were used for independent image reconstructions in phantom studies so as to optimize the choice of photopeak and image reconstruction parameters before demonstrating the abilities of ^{209}At-SPECT *in vivo*. In this way, we present ^{211}At and ^{209}At as a new, element-matched theranostic pair for preclinical therapy and imaging studies, respectively.

2. Materials and methods
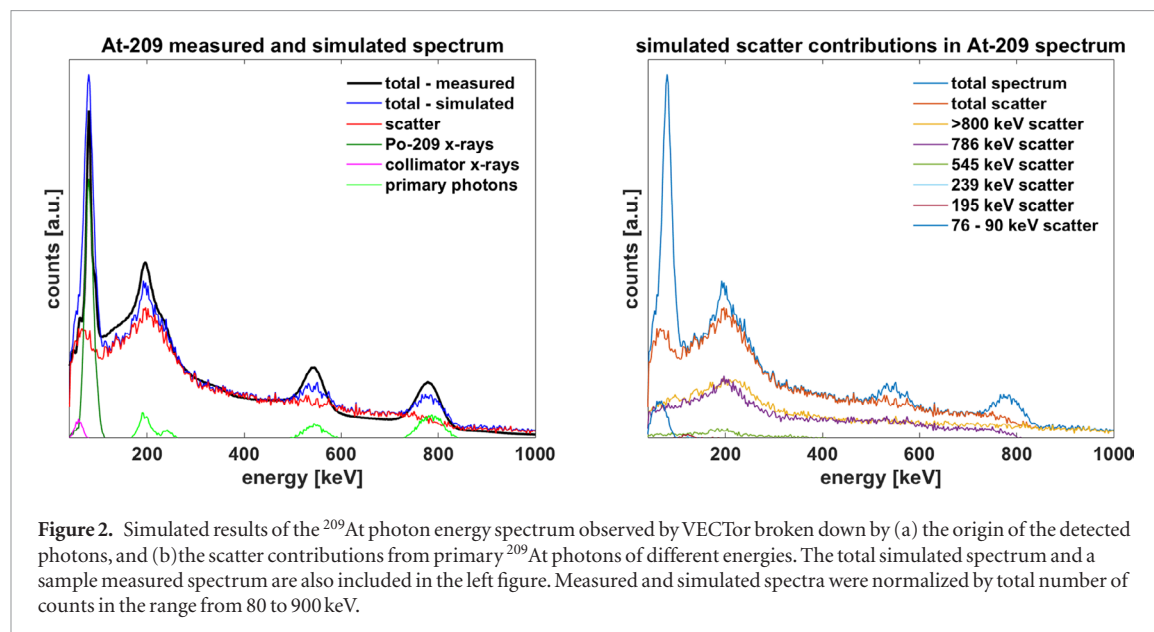
2.1. ^{209}At production

^{209}At was obtained from the decay of ^{213}Fr ($t_{1/2} = 35$ s) and ^{213}Ra ($t_{1/2} = 2.7$ min) produced at the TRIUMF ISAC Facility as previously decribed (Crawford, Kunz, Yang, Schaffer and Ruth 2017). The combined decay chain of ^{209}At, ^{213}Fr, and ^{213}Ra is shown in figure 1. Briefly, these radionuclides were produced by irradiating a uranium carbide target with 480 MeV protons at 10 μA, followed by on-line surface ionization to create a radioactive ion beam containing Fr and Ra isotopes. The $A = 213$ isobars were separated from other products via a high resolution mass separator and implanted into a thin NaCl disc. After implantation, the salt was dissolved with 0.1–2 M NaOH.

In order to purify and isolate the ^{209}At, the bulk basic solution was added to a granular tellurium (Te) column, as previously described for ^{211}At purification following analogous production methods (Bochvarova *et al* 1972, Crawford *et al* 2017a). For rapid measurement of ^{209}At quantities, a dose calibrator—cross-calibrated with known quantities of ^{209}At deteremined via gamma spectroscopy—was used, as previously described (Crawford *et al* 2017b).

2.2. SPECT data acquisition and image reconstruction

All imaging was performed with the VECTor microSPECT/PET/CT system (MILabs, Utrecht, Netherlands). VECTor is a small-animal scanner capable of single-photon imaging and equipped with an on-board x-ray CT scanner (Goorden *et al* 2012). The minimum energy for imaging with this system is 20 keV while the energy resolution is 9.3% for 140 keV and 8.6% for 511 keV. While a variety of cylindrical collimators are made available for use with VECTor, a high-energy (HE) collimator was selected for these studies given the high energy gamma emissions from ^{209}At (Miwa *et al* 2015). Designed for single-photon imaging of PET isotopes (511 keV), the HE collimator consists of a 4.0–4.5 cm thick tungsten wall with inner bore radius of 4.8 cm. 162 focused pinhole apertures surround and are focused onto a central 0.9 ml region from which SPECT data are collected. Larger volumes were imaged by translating the animal bed in the *x*, *y*, and *z* directions using a 3D helical motion. With this collimator, the system has a sensitivity of 6000 cps per MBq of ^{18}F, and a spatial resolution of 0.50 mm for 140 keV photons and 0.75 mm for 511 keV photons (Goorden *et al* 2012).

Data were collected in list-mode (where each detected emission is recorded individually, listing time, energy, etc) and binned into 512 channels of 2.34 keV width—a sample of the resulting photon energy spectrum is

Figure 2. Simulated results of the ^{209}At photon energy spectrum observed by VECTor broken down by (a) the origin of the detected photons, and (b)the scatter contributions from primary ^{209}At photons of different energies. The total simulated spectrum and a sample measured spectrum are also included in the left figure. Measured and simulated spectra were normalized by total number of counts in the range from 80 to 900 keV.

shown in figure 2. SPECT image reconstruction was performed using software provided by the scanner manufacturer. Four distinct photopeaks of the energy spectrum corresponding to the emissions of ^{209}At with the highest abundance (77–92 keV x-rays, 195 keV, 545 keV, and 782–790 keV) were individually selected for image reconstruction using energy windows of 25% width relative to the peak energy. Background and scatter correction was performed with the triple energy window method using high and low energy background windows of 20% width. Using VECTor's pixel-based ordered subset expectation maximization (POSEM) iterative reconstruction algorithm (Branderhorst *et al* 2010), decay-corrected images with 0.4 mm wide cubic voxels were reconstructed using 16 subsets and 10–15 iterations. Registration of the resulting SPECT images to CT images was performed, enabling attenuation correction of SPECT images and fused SPECT/CT viewing. These CT images were acquired immediately following SPECT data acquisition using a 55 kV voltage and 615 μA current—CT image reconstruction was performed automatically by the VECTor software. The registration of CT and SPECT images resampled the SPECT images to a grid of 0.16 mm cubic voxels. Finally, a 3D Gaussian smoothing filter (1 mm FWHM, kernel size 7) was applied to reduce noise. Quantitative SPECT images were enabled by applying a calibration factor determined via imaging of a syringe containing 32 MBq (independently determined via a Atomlab 500 dose calibrator (Biodex Medical Systems, Shirley, NY, USA) of ^{209}At uniformly distributed within a 6.5 ml volume. The reconstructed images were analyzed using MATLAB R2017a.

2.3. Monte Carlo simulation of detected ^{209}At photon energy spectrum

In order to investigate components in the photon energy spectrum attributable to scatter from high energy emissions from ^{209}At, the ^{209}At energy spectrum detected by VECTor was further evaluated by Monte Carlo simulation using GATE (Geant4 Application for Emission Tomography, v6.1) (Jan *et al* 2004). For this simulation, the high-energy collimator geometry was approximated as a 4.3 cm thick tungsten cylinder containing 15 equally spaced 0.7 mm diameter pinholes with opening angle of 16 degrees, arranged in a single ring and focused on a 1 mm diameter water sphere containing a uniform ^{209}At activity distribution. The pinhole geometry (0.7 mm diameter, 16 degree opening angle) was obtained from Goorden *et al* (2012). While this model geometry did not entirely reflect the physical geometry of the collimator, which contains 4 rings of clustered 0.7 mm diameter pinholes, it was used to approximate the general features of the measured ^{209}At spectrum as related to photon peak detection and scatter contributions.

The detector system was modelled as three 9.5 cm thick NaI detectors arranged in triangular geometry covered by a 0.05 cm thick aluminum layer at the front and a 6.6 cm thick back-compartment region. Additionally, three lead panels (3 cm thickness) were placed behind the back-compartment region to model the shielding material around the system. The NaI energy resolution was modelled as 9% at 511 keV. Additional details of this Monte-Carlo model can be found in Esquinas *et al* (2017).

The ^{209}At decay data was built-in in GATE, and it is based on the evaluated nuclear structure data file (ENDSF) database (Bhat 1992). In addition to nuclear decay, the simulation included photoelectric effects, Compton and Rayleigh scattering, pair-production, electron ionization and scattering, electron–positron annihilation and Bremsstrahlung. A total of 2×10^8 nuclear decays were simulated. Only detected photons with energies between 40 keV and 2000 keV were recorded.

2.4. Image uniformity and spatial resolution

Dedicated image quality phantoms were used to assess and compare the quality of images reconstructed from data acquired in the different photopeaks. Image uniformity was assessed using a phantom consisting of a 12 ml syringe filled with 6.5 ml of [^{209}At]astatide (32 MBq, uniformly distributed), for which SPECT data was acquired for 60 min. Transverse line profiles drawn through the central axis of the phantom images were used to illustrate image uniformity. Image uniformity was quantified as the ratio of standard deviation to mean value (%SD) for voxels contained within a cylindrical ROI (10 mm diameter, 20 mm height) positioned concentric to the activity distribution ($\%SD = \sigma/\bar{\mu}\times100\%$).

Spatial resolution was estimated using an acrylic hotrod phantom containing groups of rods with diameters of 0.85, 0.95, 1.10, 1.30, 1.50, and 1.70 mm, with each rod in a group separated by two times its diameter, measured centre to centre. The rods were loaded with an aqueous solution (0.1 M NaOH) of [^{209}At]astatide (4.1 MBq ml^{-1}) for a total activity in the phantom of 2.9 MBq. SPECT data was acquired for 3 h. Images reconstructed for each of the four photopeaks were analyzed following the procedure defined by Walker *et al* (Walker *et al* 2014), where for each group of rods of equal diameter the contrast between ROIs centred on rods and ROIs centred between rods was used to parameterized the image resolution. A threshold of 20% contrast was used to define resolvability.

2.5. *In vivo* imaging and biodistribution studies

All animal studies were performed in accordance with the Animal Care Committee (ACC) of the University of British Columbia under the approved protocol A16-0150. A healthy C57bl6 mouse (Charles River Laboratories, St. Constant, QC, Canada) was injected with free ^{209}At$^-$ in order to compare its resulting biodistribution with the well-known biodistribution of free astatide, which typically sequesters in the thyroid, stomach, lungs, salivary glands, and urine (Larsen *et al* 1998). [^{209}At]astatide extracted from the Te column in 2 M NaOH (Crawford *et al* 2017b) was neutralized by the addition of minimal 0.1–1 M HCl and diluted in saline. The mouse was anaesthetized and administered 10 MBq in 200 μl via tail-vein injection. Beginning at 30 min post-injection, whole-body dynamic SPECT imaging was performed using a total of 20 consecutive frames of 5 min acquistions per frames. Respiratory rate and temperature were monitored constantly during the scan, and isoflurane and bed temperature adjusted accordingly. Following SPECT/CT data acquisition, the mouse was sacrificed by isoflurane overdose and cardiac puncture.

Within the reconstructed SPECT images, *in vivo* measurements of percent injected dose per gram (%ID/g) were determined for organs of interest using ellipsoidal regions of interest (ROIs), manually placed around individual organs. In order to validate SPECT-based biodistribution measurements, *ex vivo* assessment of the ^{209}At biodistribution was determined by removing organs of interest and counting them in a NaI) Packard Cobra II auto-gamma counter (Canberra-Packard Canada Ltd, Mississauga, ON, Canada), using a broad energy window (410–680 keV), corresponding to the 545 keV photopeak, and counting for 1 minute per organ. The detector was cross-calibrated with the dose calibrator using 1 ml aliquots of ^{209}At$^-$ (in water) in order to determine %ID/g for each organ.
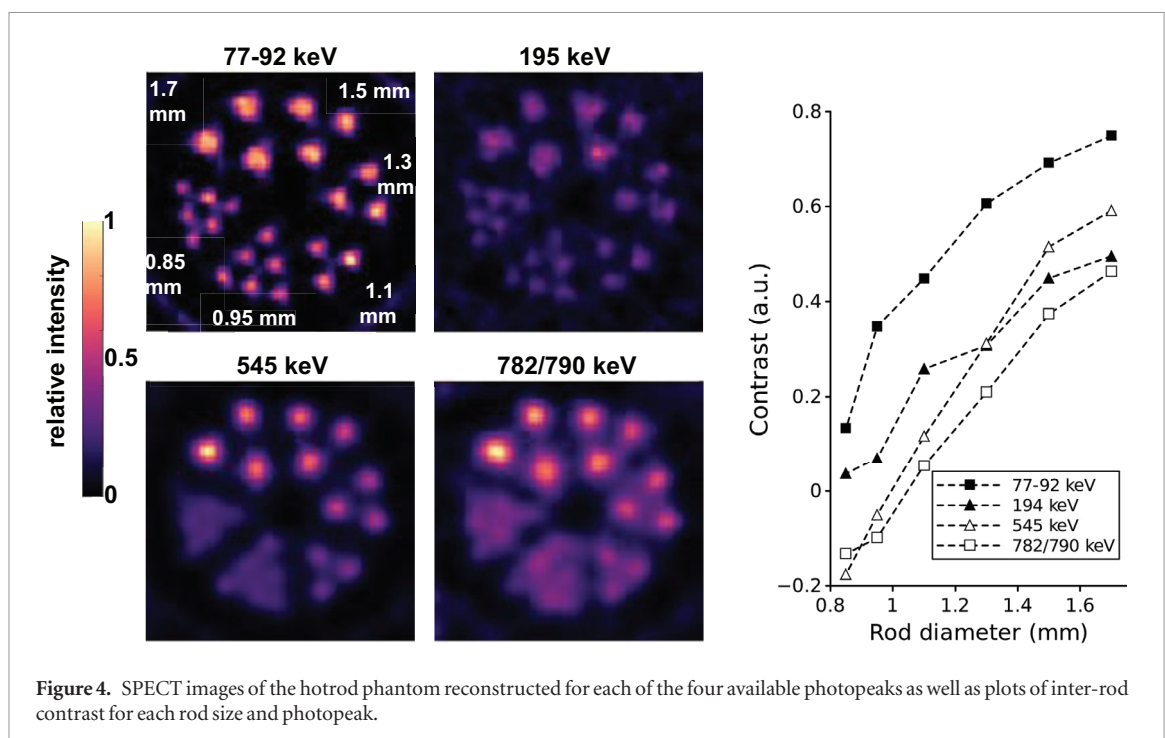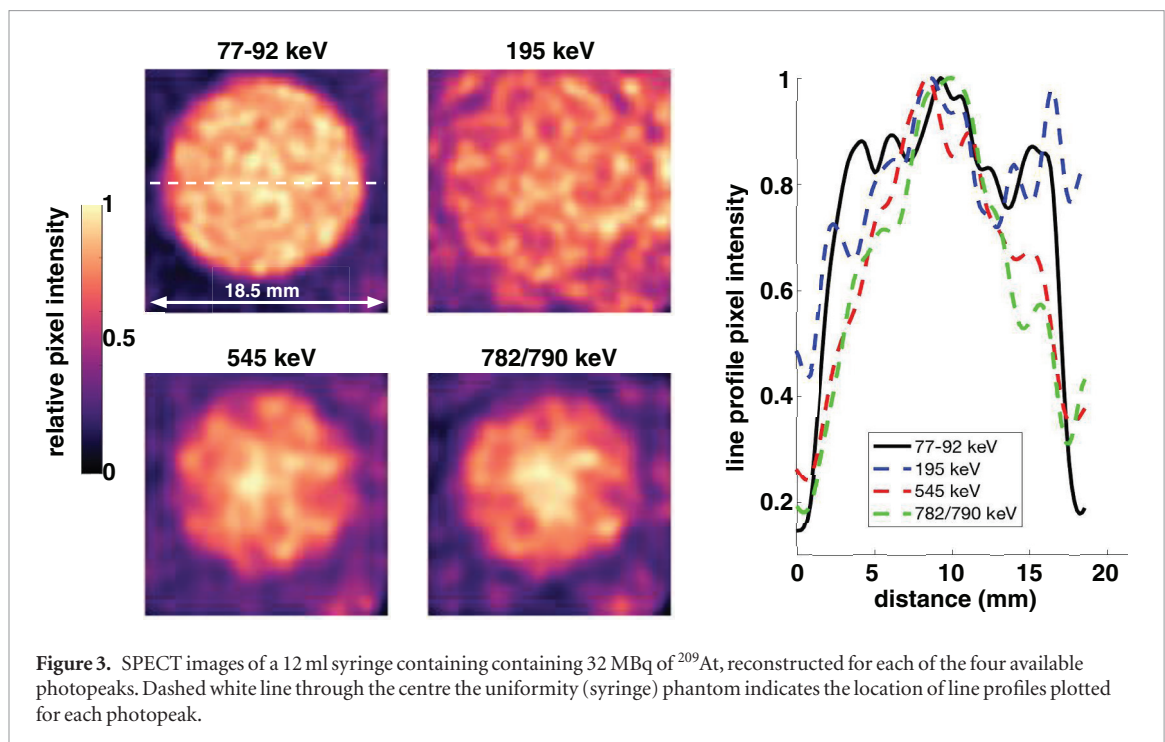
3. Results

3.1. Evaluation of photon energy spectrum for ^{209}At imaging with VECTor

The sample photon energy spectrum shown in figure 2(a) illustrates the three distinct ^{209}At gamma peaks (195, 545, and 782/790 keV, with intensities of 24%, 91%, and 83%/64%, respectively) and the combined peak of Po x-rays (77–90 keV) available for imaging. The background appeared much higher at lower energies between 100–300 keV, completely obscuring the 240 keV (13%) ^{209}At peak. Additionally, the nearby 195 keV peak appears broadened and asymmetrical, the first indication this peak is poorly suited for imaging due to the amount of Compton scattering photons present in this energy region.

Details of the origin of this high scatter component are revealed by the GATE simulations. Figure 2(a) also shows a comparison of the measured and simulated photon energy spectrum. Visually, the two spectra appear to agree well, with the exception of a larger x-ray peak in the simulated spectrum and a misalignment of the peaks due to a known drift in the VECTor energy calibration at the time of data collection. Decomposition of simulated spectrum components into primary and scattered photons figure 2(a) highlights that the 195 keV peak is sitting on the dominant backscatter peak. Figure 2(b) further illustrates that this backscatter peak is primarily the result of the high (>750 keV) photons emitted by ^{209}At.
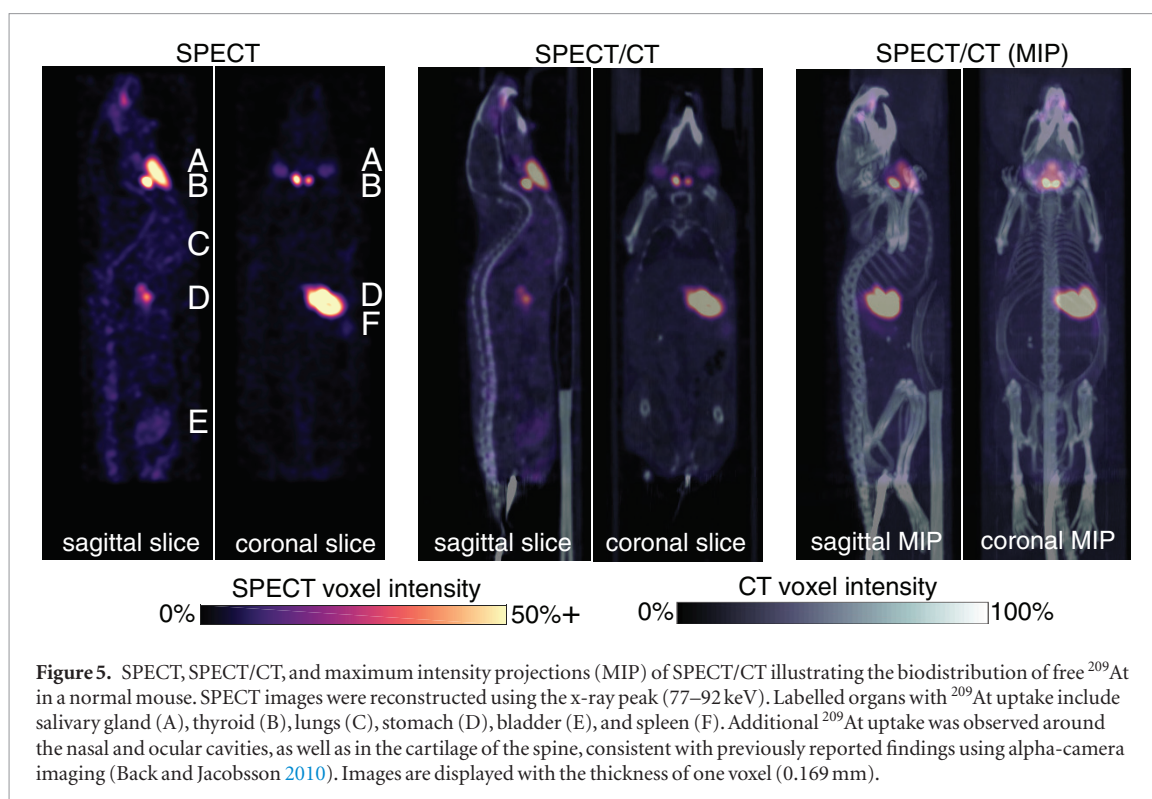
3.2. Image uniformity and spatial resolution

Individual images of the uniformity phantom reconstructed using each of the ^{209}At photopeaks are shown in figure 3. Qualitatively, the 77–90 keV image was superior to all other images. Transverse line profiles through the central axis of the uniform ^{209}At activity distribution (also shown in figure 3) illustrate the variation in voxel

Figure 3. SPECT images of a 12 ml syringe containing containing 32 MBq of ^{209}At, reconstructed for each of the four available photopeaks. Dashed white line through the centre the uniformity (syringe) phantom indicates the location of line profiles plotted for each photopeak.

Figure 4. SPECT images of the hotrod phantom reconstructed for each of the four available photopeaks as well as plots of inter-rod contrast for each rod size and photopeak.

intensity for reconstructions made using each photopeak. Again, the 77–90 keV profiles look best, with the edge of the syringe clearly defined (unlike the 195 keV image), and a uniform intensity within the syringe (unlike the 545 keV and 790 keV profiles which contain high intensity peaks within at the syringe centre). Central ROI were found to have %SD values of 17%, 24%, 19%, and 22%, for 77–92 keV, 195 keV, 545 keV, and 782/790 keV image reconstructions, respectively.

Images of the resolution phantom reconstructed with each photopeak are shown in figure 4. Again, image quality visually appears best for images reconstructed with the x-ray peak. Assessment of inter-rod contrast (also shown in figure 4) quantitatively supports this, as all rod sizes were resolved in the x-ray peak, while rods ⩾0.95 mm were resolved with the 195 keV peak and rods ⩾1.3 mm were resolved in the 545 keV and combined 782/790 keV peaks.

Figure 5. SPECT, SPECT/CT, and maximum intensity projections (MIP) of SPECT/CT illustrating the biodistribution of free ^{209}At in a normal mouse. SPECT images were reconstructed using the x-ray peak (77–92 keV). Labelled organs with ^{209}At uptake include salivary gland (A), thyroid (B), lungs (C), stomach (D), bladder (E), and spleen (F). Additional ^{209}At uptake was observed around the nasal and ocular cavities, as well as in the cartilage of the spine, consistent with previously reported findings using alpha-camera imaging (Back and Jacobsson 2010). Images are displayed with the thickness of one voxel (0.169 mm).

3.3. *In vivo* studies

Given the superior quality of images reconstructed using the x-ray peak (see section 3.2), all *in vivo* image analysis was performed using images only reconstructed by this peak. Figure 5 shows *in vivo* SPECT images of the mouse injected with free [^{209}At]astatide, reconstructed using all data from all 20 frames collected between 30 and 160 min post-injection. These images visualize the expected ^{209}At biodistribution (Larsen *et al* 1998), with the thyroid, stomach, salivary glands, lungs, spleen, and bladder showing visible uptake. Quantitative *ex vivo* biodistribution provided confirmation of the activity distributed to these organs, as shown in figure 6, which also illustrates changes in the ^{209}At biodistribution over time captured by the dynamic reconstructions for each of the individual 5 minute frames. Extrapolation of the SPECT-based measurement of total ^{209}At in each organ agreed with *ex vivo* whole-organ counting measurements within 10%, with the exception of the stomach. *Ex vivo* stomach measurements appear slightly lowered, a result expected since some stomach contents were removed before counting the organ.

4. Discussion

Both the measured and simulated ^{209}At spectra seen by VECTor figure 2(a) suggest that the x-ray peak provides the best option for ^{209}At image reconstruction due to the large number of available counts—a result of the high branching ratio and high detection efficiency by NaI for photons of that energy, when compared to the other available peaks (195, 545, and 782/790 keV). This observation is further supported by the phantom imaging studies: uniformity profiles figure 3 and spatial resolution figure 4 appear superior for images reconstructed with this peak. The superior spatial resolution at lower energies is an expected result, as spatial resolution is known to decrease at higher energies for VECTor (Goorden *et al* 2012, Robertson *et al* 2017). Considering other peaks, the poor performance of the 782/790 keV peak is possibly attributable to collimator pinhole edge penetration, as these photons are well above the typical energy range of this collimator (⩽511 keV). The hotrod phantom images reconstructed with the 545 keV peak exhibit a spatial resolution (1.3 mm) that is worse than typically observed in VECTor images at this energy (0.80 mm for 511 keV (Goorden *et al* 2012)). While the source of this discrepancy is not clear, it is likely that the point spread function of the ^{209}At 545 keV photopeak is wider than a pure 511 keV photopeak due to contributions from higher energy emissions exhibiting collimator edge penetration, resulting in a loss of resolution. Better image contrast for 545 keV reconstructions is likely achievable using detector materials that offer better energy resolution, as compared to NaI(Tl), such as LaBr$_3$(Ce).

The observed spatial resolution for the x-ray peak images (⩽0.85 mm) is consistent with reported results for imaging at low energies with VECTor (0.50 mm for 140 keV (Goorden *et al* 2012)). Uniformity profiles for the 545 and 782/790 keV peaks also appear less uniform and less clearly indicate the edge of the syringe phantom than do the profiles for the x-ray peak images. The 545 and 782/790 keV uniformity phantom images also present
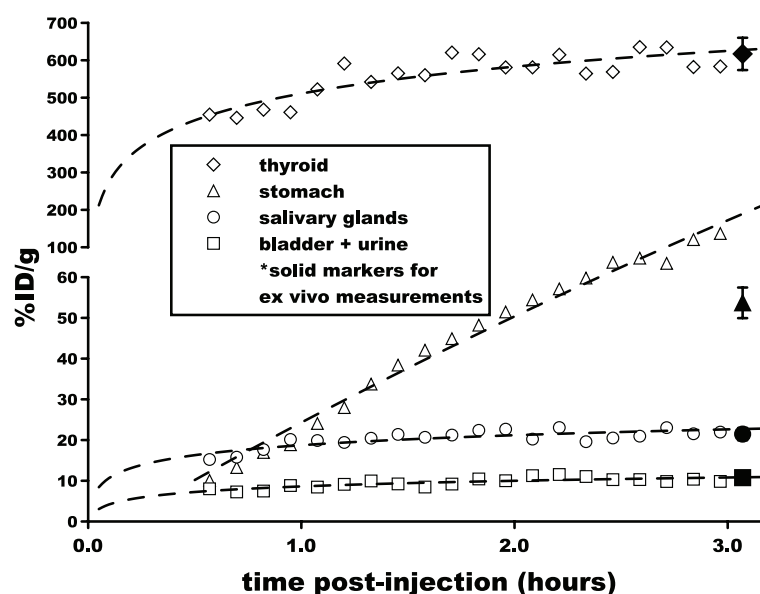
Figure 6. Measurements of total ^{209}At activity in organs of interest determined both from dynamic SPECT images reconstructed from the x-ray peak and from *ex vivo* measurements conducted after imaging. *Ex vivo* measurements are the final data point for each organ (solid markers), while *in vivo* measurements (outlined markers) make up the remaining values. Trendlines (dashes) for each organ were fit with functions of the form $y = a + b\ln(x + c)$.

artefacts characterized by a high intensity spot in the centre of the phantom, possibly a result of collimator edge penetration, down-scatter, or over-correcting for attenuation. Even with reduced image quality, imaging with high energy photopeaks may be necessary for larger animals where the proportionately higher linear attenuation of 77–92 keV x-rays will be most significant, resulting in lower counts for reconstruction. Attenuation effects for ^{209}At emissions requires further evaluation.

The low quality of 195 keV images—for which image uniformity and spatial resolution are the worst—can be attributed to the fact that this peak sits on the backscatter peak arising from Compton scattering photons of the highest energies (>750 keV), by far the most significant scatter contributions in the ^{209}At spectrum, as revealed by the GATE simulation results in figure 2. Though differences exist between the total measured and simulated ^{209}At energy spectra in the x-ray region—an energy region for which GATE simulations are known to be less accurate and more sensitive to inaccuracies of the simulated geometry—the spectra compare well enough at higher energies to suggest that these simulations accurately model ^{209}At gamma ray interactions within the VECTor scanner despite approximations made to the simulated geometry. The complexity of the spectrum and the amount of scatter in the region of the 195 keV peak are likely the cause of the poor image quality of images reconstructed using this peak. While the triple-energy-window scatter correction method used by the VECTor reconstruction algorithm is known to be capable of appropriate correcting for scatter effects, this does not appear to be the case for the 195 keV ^{209}At peak, for which scattered photons are reconstructed—an effect most visible in the 195 keV uniformity phantom image figure 3 where the edge of the syringe is not clearly visible, with much activity reconstructed outside the syringe.

The *in vivo* ^{209}At images shown in figure 5 illustrate the potential of this x-ray peak to visualize At biodistributions, while the comparison with *ex vivo* measurements in figure 6 indicates that quantitative biodistribution measurements determined from ^{209}At SPECT images are consistent with conventional *ex vivo* biodistribution measurements, even when imaging data is acquired over short 5 min frames. These quantitatively accurate ^{209}At SPECT images determined At time-activity curves using a single animal subject, a clear complement to *ex vivo* methods which only provide a snapshot of the At biodistribution at the time of sacrifice and require multiple subjects in order to determine time-activity curves. The spatial resolution of images reconstructed using the x-ray peak ($\leqslant 0.85$ mm) also implies that, compared to *ex vivo* biodistribution measurements, these image-based methods have potential to provide additional information about the 3D At distribution at the sub-organ level. Though only demonstrated in a normal mouse with free [^{209}At]astatide, these image-based biodistribution measurements have potential to quantitatively determine the pharmacokinetics of At-labelled compounds with high time-resolution. This is of particular interest to the [^{211}At]astatinated small molecules and peptides used as radiotherapeutics, where fast biokinetics significantly impact the dose distribution and the resulting damage to healthy organs.

This work demonstrates the theranostic abilities of the ^{209}At/^{211}At isotope pair. While ^{209}At imaging is challenged by the currently limited availability of ^{209}At (Crawford *et al* 2017a) and the need for a high energy col-

limator not found on most preclinical SPECT scanners, ^{209}At imaging offers advantages over other previously described methods that image ^{211}At x-ray emissions. These advantages include a three-fold higher total branching ratio of x-ray emissions from ^{209}At over ^{211}At table 1, and a 25-fold lower alpha emission rate that reduces toxicity and may permit the use of the higher activities needed for imaging. As shown in figure 1, four alpha emissions result from every 100 ^{209}At decays, while every ^{211}At decay results in an alpha emission, either by direct alpha decay to ^{207}Bi or indirectly via the rapid decay of its daughter, ^{211}Po. While ^{209}At decays to the alpha-emitter ^{209}Po, the long ^{209}Po half-life ($t_{1/2} = 102$ y) reduces the dose rate and therefore the biological effects. For example, a 10 MBq injection of ^{209}At produces only 60 Bq of ^{209}Po. In addition, larger high energy collimators will also need to be compatible with the abundant 545 keV and 782/790 keV emissions of ^{209}At. By providing accurate images of the At biodistribution with high temporal and spatial resolution, SPECT imaging with ^{209}At has potential to provide valuable information relevant to the development of ^{211}At-radiopharmaceuticals.

5. Conclusion

We have demonstrated the ability of quantitative SPECT imaging with ^{209}At—a novel imaging isotope—to accurately determine astatine biodistributions with high temporal resolution. For small animal imaging, x-ray reconstructions were shown to provide sub-organ spatial resolution (<0.85 mm). High energy gammas (545 keV), exhibiting much less attenuation by tissue, are expected to be most useful for imaging astatine activity distributions in larger animals.

Acknowledgments

ORCID iDs

A K H Robertson ⓘ https://orcid.org/0000-0003-4154-6176

References

Andersson H *et al* 2009 Intraperitoneal alpha-particle radioimmunotherapy of ovarian cancer patients: pharmacokinetics and dosimetry of ^{211}At-MX35 F(ab')$_2$—a Phase I study *J. Nucl. Med.* **50** 1153–60

Back T and Jacobsson L 2010 The alpha-camera: a quantitative digital autoradiography technique using a charge-coupled device for *ex vivo* high-resolution bioimaging of alpha-particles *J. Nucl. Med.* **51** 1616–23

Back T, Chouin N, Lindegren S, Jensen H, Albertsson P and Palm S 2014 Image-based small-scale 3D-dosimetry in targeted alpha therapy using voxel dose-point kernels and alpha camera imaging of serial tissue sections *J. Nucl. Med.* **55** (suppl. 1) 50

Baidoo K E, Yong K and Brechbiel M W 2013 Molecular pathways: targeted alpha-particle radiation therapy *Clin. Cancer Res.* **19** 530–7

Bhat M R 1992 Evaluated nuclear structure data file (ENSDF) *Nuclear Data for Science and Technology* (Berlin: Springer) pp 817–21

Bloomer W D, McLaughlin W H, Neirinckx R D, Adelstein S J, Gordon P R, Ruth T J and Wolf A P 1981 Astatine-211–Tellurium radiocolloid cures experimental malignant ascites *Science* **212** 340–1

Bochvarova M, Tyung D, Dudova I, Norseev Y and Khalkin V 1972 Investigation of columns filled with crystalline tellurium for the production of radiochemically pure preparations of astatine *Radiokhimiya* **14** 881–95

Branderhorst W, Vastenhouw B and Beekman F J 2010 Pixel-based subsets for rapid multi-pinhole SPECT reconstruction *Phys. Med. Biol.* **55** 2023–34

Brechbiel M 2007 Targeted alpha-therapy: past, present, future? *Dalton Trans.* **43** 4918–28

Chouin N, Lindegren S, Jensen H, Albertsson P and Bäck T 2012 Quantification of activity by alpha-camera imaging and small-scale dosimetry within ovarian carcinoma micrometastases treated with targeted alpha therapy *Q. J. Nucl. Med. Mol. Imaging* **56** 487–95

Couturier O, Supiot S, Degraef-Mougin M, Faivre-Chauvet A, Carlier T, Chatal J F, Davodeau F and Cherel M 2005 Cancer radioimmunotherapy with alpha-emitting nuclides *Eur. J. Nucl. Med. Mol. Imaging* **32** 601–14

Crawford J R, Kunz P, Yang H, Schaffer P and Ruth T J 2017a ^{211}Rn/^{211}At and ^{209}At production with intense mass separated Fr ion beams for preclinical ^{211}At-based α-therapy research *Appl. Radiat. Isot.* **122** 222–8

Crawford J R, Yang H, Kunz P, Wilbur S, Schaffer P and Ruth T J 2017b Development of a preclinical ^{211}Rn/^{211}At generator system for targeted alpha therapy research with ^{211}At *Nucl. Med. Biol.* **48** 31–5

Elgqvist J, Frost S, Pouget J P and Albertsson P 2014 The potential and hurdles of targeted alpha therapy—clinical trials and beyond *Front. Oncol.* **3** 324

Esquinas P L *et al* 2017 ^{188}Re image performance assessment using small animal multi-pinhole SPECT/PET/CT system *Phys. Med.* **33** 26–37

Gilland D R, Jaszczak R J, Greer K L and Coleman R E 1991 Quantitative SPECT reconstruction of Iodine-123 data *J. Nucl. Med.* **32** 527–33

Goorden M C, van der Have F, Kreuger R, Ramakers R M, Vastenhouw B, Burbach J P H, Booij J, Molthoff C F M and Beekman F J 2012 VECTor: a preclinical imaging system for simultaneous submillimeter SPECT and PET *J. Nucl. Med.* **54** 306–12

Jan S *et al* 2004 GATE: a simulation toolkit for PET and SPECT *Phys. Med. Biol.* **49** 4543–61

Johnson E L, Turkington T G, Jaszczak R J, Gilland D R, Vaidyanathan G, Greer K L, Coleman R E and Zalutsky M R 1995 Quantitation of ^{211}At in small volumes for evaluation of targeted radiotherapy in animal models *Nucl. Med. Biol.* **22** 45–54

Kim Y and Brechbiel M W 2012 An overview of targeted alpha therapy *Tumor Biol.* **33** 573–90

Larsen R H, Slade S and Zalutsky M R 1998 Blocking [²¹¹At]astatide accumulation in normal tissues: preliminary evaluation of seven potential compounds *Nucl. Med. Biol.* **25** 351–7

Macey D J, DeNardo G L, DeNardo S J and Hines H H 1986 Comparison of low- and medium-energy collimators for SPECT imaging with Iodine-123-labeled antibodies *J. Nucl. Med.* **27** 1467–74

McDevitt M R, Sgouros G, Finn R D, Humm J L, Jurcic J G, Larson S M and Scheinberg D A 1998 Radioimmunotherapy with alpha-emitting nuclides *Eur. J. Nucl. Med.* **25** 1341–51

Miller B W *et al* 2015 Quantitative single-particle digital autoradiography with α-particle emitters for targeted radionuclide therapy using the iQID camera *Med. Phys.* **42** 4094–105

Miller B W, Gregory S J, Fuller E S, Barrett H H, Bradford Barber H and Furenlid L R 2014 The iQID camera: an ionizing-radiation quantum imaging detector *Nucl. Instrum. Methods Phys. Res.* A **767** 146–52

Miwa K, Inubushi M, Takeuchi Y, Katafuchi T, Koizumi M, Saga T and Sasaki M 2015 Performance characteristics of a novel clustered multi-pinhole technology for simultaneous high-resolution SPECT/PET *Ann. Nucl. Med.* **127** 460–6

Mulford D, Scheinberg D and Jurcic J 2005 The promise of targeted α-particle therapy *J. Nucl. Med.* **46** 199S–204S

National Nuclear Data Center 2017 NuDat 2.7. Nuclear Structure and Decay Data (Retrieved September 2017, from http://www.nndc.bnl.gov/nudat2/)

Orozco J *et al* 2013 Anti-CD45 radioimmunotherapy using the alpha-emitting radionuclide ²¹¹At combined with bone marrow transplantation prolongs survival in a disseminated murine leukemia model *Blood* **121** 3759–68

Polak J F, Holman B L, Moretti J L, Eisner R L, Lister-James J and English R J 1984 I-123 HIPDM brain imaging with a rotating gamma camera and slant-hole collimator *J. Nucl. Med.* **25** 495–8

Robertson A K H, Ramogida C, Rodríguez-Rodríguez C, Blinder S, Kunz P, Sossi V and Schaffer P 2017 Multi-isotope SPECT imaging of the ²²⁵Ac decay chain: feasibility studies *Phys. Med. Biol.* **62** 4406–20

Sgouros G, Hobbs R F and Song H 2011 Modelling and dosimetry for alpha-particle therapy *Curr. Radiopharm.* **4** 261–5

Sgouros G, Roeske J C, McDevitt M R, Palm S, Allen B J, Fisher D R, Brill A B, Song H, Howell R W and Akabani G 2010 MIRD Pamphlet No. 22: radiobiology and dosimetry of alpha-particle emitters for targeted radionuclide therapy *J. Nucl. Med.* **51** 311–28

Turkington T G, Sontag M R and Jaszczak R J 1993 Measuring astatine-211 distributions with SPECT *Phys. Med. Biol.* **38** 1121–30

Walker M D, Goorden M C, Dinelle K, Ramakers R M, Blinder S, Shirmohammad M, van der Have F, Beekman F J and Sossi V 2014 Performance assessment of a preclinical PET scanner with pinhole collimation by comparison to a coincidence-based small-animal PET scanner *J. Nucl. Med.* **55** 1368–74

Zalutsky M R, Reardon D A, Akabani G, Coleman R E, Friedman H, Friedman H S, Mclendon R E, Wong T Z and Bigner D 2008 Clinical experience with alpha-particle-emitting ²¹¹At: treatment of recurrent brain tumor patients with 211At-labeled chimeric antitenascin monoclonal anitbody 81C6 *J. Nucl. Med.* **49** 30–8